

Self-Activated Cascade Biocatalysis of Glucose Oxidase–Polycation–Iron Nanoconjugates Augments Cancer Immunotherapy

Fei Duan, Wei Jin, Tong Zhang, Fan Zhang, Like Gong, Xinyu Liu, Xuliang Deng,* and Weiping Gao*



Cite This: *ACS Appl. Mater. Interfaces* 2022, 14, 32823–32835



Read Online

ACCESS |



Metrics & More



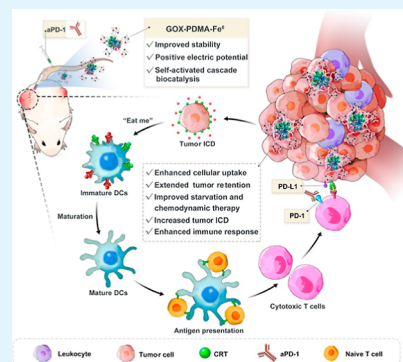
Article Recommendations



Supporting Information

ABSTRACT: Biocatalytic therapy by reactive-oxygen-species-generating enzymes not only kills cancer cells directly but also stimulates an anticancer immune response and inverses the immunosuppressive microenvironment of a variety of solid tumors, which is potentially beneficial to overcoming the limitations of cancer immunotherapy. Herein, we report the in situ growth of polycation chains from glucose oxidase to generate glucose oxidase–polycation conjugates, which can be used as a template for the in situ reduction of ferrous ions into iron nanoparticles to yield glucose oxidase–polycation–iron nanoconjugates. The nanoconjugates exhibit enhanced cellular uptake and cancer retention as well as self-activated cascade biocatalysis that consumes glucose and generates highly toxic hydroxyl radicals, leading to enhanced starvation-like and chemodynamic cancer therapy. The cancer treatment with the nanoconjugates efficiently triggers the program of immunogenic cell death for enhanced immune checkpoint blockade therapy. The synergy of self-activated cascade biocatalysis and immune checkpoint blockade not only eradicates primary cancers but also inhibits the progression of distant cancers, which leads to the abscopal effect on cancers. Our findings provide a method for the in situ synthesis of self-activated cascade nano-biocatalysts for cascade biocatalysis-enhanced immunotherapy of cancer.

KEYWORDS: glucose oxidase, enzyme-polymer conjugate, nanoconjugate, biocatalysis, cancer immunotherapy



INTRODUCTION

Cancer immunotherapy has become a new paradigm of cancer treatment besides surgery, radiation, and chemotherapy.^{1–5} Nevertheless, poor immunogenicity and the immunosuppressive microenvironment of cancer often lead to the low response rate of cancer immunotherapy in clinic.^{6–8} To address these problems, efforts have been directed to immunogenic cell death (ICD).⁹ In ICD, the dying tumor cells overexpress and release danger-associated molecular patterns, proinflammatory cytokines, and tumor-associated antigens, which stimulate antigen-specific immune responses and augment the activation, proliferation, and tumor infiltration of T cells.^{10,11} Reactive oxygen species (ROS) have extensively been studied to efficiently elicit ICD. To date, several ROS-generating strategies, including chemotherapy, phototherapy, radiotherapy, and catalytic therapy, have been developed to induce ICD for improved cancer immunotherapy.^{12–20} These strategies are used typically in combination with immune checkpoint blockade (ICB) therapy to maximize the anticancer efficacy.²⁰

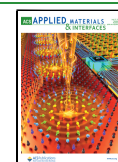
ROS-generating enzymes, including glucose oxidase (GOX), xanthine oxidase, and D-amino acid oxidase, have been explored for biocatalytic therapy of cancer.^{21–25} As a prime example, GOX catalyzes the conversions of glucose into gluconic acid and oxygen (O₂) into hydrogen peroxide

(H₂O₂). The glucose depletion and H₂O₂ generation have been exploited for starvation-like and chemodynamic therapy of cancer.^{21,22} Nevertheless, GOX suffers from low stability, a short circulatory half-life, systemic toxicity, and immunogenicity. To solve these problems of GOX, a number of GOX formulations have been developed, including GOX-conjugated microspheres,²¹ GOX–polymer conjugates^{22,26} or nanogels,²⁷ GOX-loaded nanomaterials,^{28–32} and cell membrane-coated GOX-loaded nanomaterials.^{33,34} Most recently, GOX-loaded nanomaterials and cancer cell membrane-coated GOX-loaded nanomaterials have been demonstrated to induce ICD for enhanced cancer immunotherapy.^{35–37} However, these GOX-based nanomedicines suffer from either the low cytotoxicity of H₂O₂ or the poor tumor-targeting and tumor-penetrating efficiency after systemic administration, leading to the low induction of ICD and the suboptimal therapeutic efficacy. Moreover, the so-called enhanced permeability and retention

Received: March 19, 2022

Accepted: July 6, 2022

Published: July 18, 2022



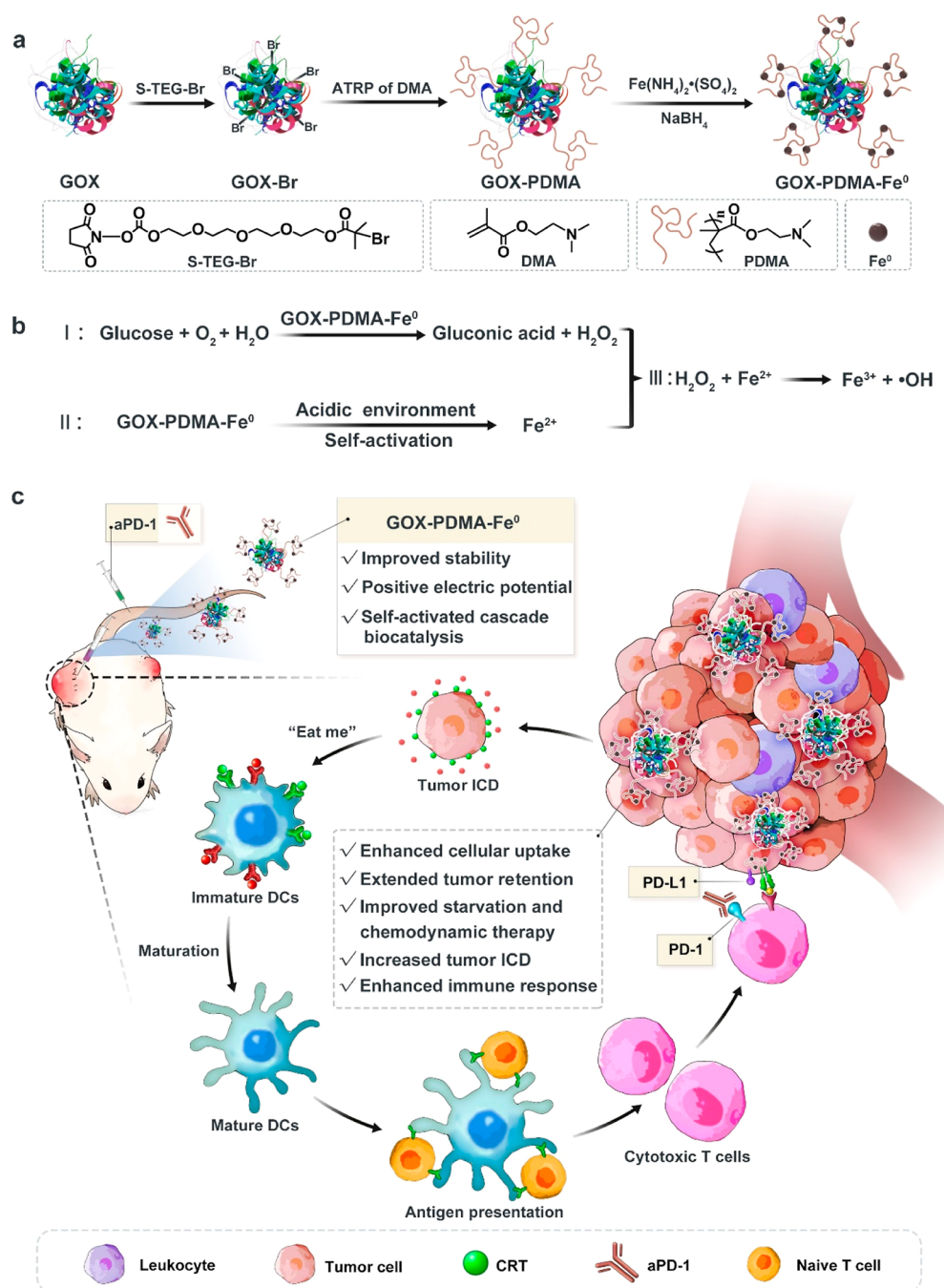


Figure 1. Scheme of the in situ synthesis of GOX-PDMA-Fe⁰ as self-activated cascade nanobiocatalysts for cascade biocatalysis-enhanced cancer immunotherapy. (a) Synthetic route of GOX-PDMA-Fe⁰. (b) Proposed mechanism of self-activated cascade biocatalysis of GOX-PDMA-Fe⁰. (c) Proposed mechanism of cascade biocatalysis-enhanced cancer immunotherapy by the combination of GOX-PDMA-Fe⁰ with anti-programmed cell death protein 1 antibody (aPD-1). DCs: dendritic cells; PD-L1: ligand for PD-1; and CRT: calreticulin.

effect has recently been demonstrated to scarcely exist,³⁸ which prevents the clinical translation of the nanomedicines.

In this study, we present the in situ synthesis of GOX-poly(*N,N'*-dimethylamino-2-ethyl methacrylate)-iron nanoconjugates (GOX-PDMA-Fe⁰) as self-activated cascade nanobiocatalysts for both cascade biocatalysis therapy and cascade biocatalysis-enhanced cancer immunotherapy. PDMA is directly grown from GOX to form GOX-PDMA conjugates, followed by the in situ formation of GOX-PDMA-Fe⁰ nanoconjugates (Figure 1a). Because the pK_a of PDMA (around 7.8) is higher than the pH of the tumor microenvironment (ca. 6.5–6.9), the PDMA block of the nano-

conjugates can be protonated to become positively charged upon intratumoral injection. Considering the electrostatic interaction between cancer cells whose membrane surfaces are negatively charged and the positively charged nanoconjugates, the nanoconjugates can be adsorbed onto cancer cells and then endocytosed after intratumoral injection to show enhanced tumor retention over GOX. Simultaneously, the GOX block of the nanoconjugates depletes glucose and generates H₂O₂ for starvation-like therapy and chemodynamic therapy, respectively (Figure 1b). The in situ formation of gluconic acid further decreases the local pH of the nanoconjugates, which can facilitate the ionization of Fe⁰ nanoparticles into ferrous

ions (Fe^{2+}) for the production of highly toxic hydroxyl radicals ($\cdot\text{OH}$) from H_2O_2 via the Fenton reaction, resulting in enhanced chemodynamic therapy and increased ICD induction. We further demonstrate that the combination of the self-activated cascade nanobiocatalysts and an immune checkpoint inhibitor leads to the dramatically enhanced anticancer efficacy (Figure 1c).

MATERIALS AND METHODS

Materials. GOX and ammonium iron(II) sulfate were purchased from Sigma-Aldrich. *N,N'*-Dimethylamino-2-ethyl methacrylate (DMA), methyl thiazolyl tetrazolium (MTT), proteinase K, fluorescein isothiocyanate (FITC), and 2',7'-dichlorofluorescein diacetate (DCFH-DA) were obtained from Aladdin. Sulfo-Cy7-NHS was purchased from Xi'an Ruixi Biological Technology (China). S-TEG-Br was synthesized according to our previously reported work.³⁹ RPMI 1640 medium and fetal bovine serum (FBS) were purchased from Gibco. Hoechst 33342 and DiD were provided by Beyotime Biotechnology (China). Anti-mouse CD86-PE, anti-mouse CD80-APC, anti-mouse CD3-APC, anti-mouse CD8-PE, mouse interferon gamma (IFN- γ) ELISA Kit, and mouse tumor necrosis factor alpha (TNF- α) ELISA Kit were purchased from Elabscience Biotechnology (China). Anti-mouse-GRP78 and rabbit anti-mouse-CRT were obtained from Abcam. Anti-mouse-PD-1 was purchased from Bioxcell. Murine mammary carcinoma (4T1) cells were purchased from the cell bank of Chinese Academy of Medical Sciences. Female BALB/c mice (6–8 weeks old) used in the experiments were purchased from the Department of Laboratory Animal Science, Peking University Health Science Center.

Synthesis of GOX–Br. Representatively, GOX (100 mg, 0.69 μmol) was dissolved into 20 mL PBS (pH 7.4, 10 mM). S-TEG-Br (3.5 mg, 0.72 μmol) was dissolved in 200 μL DMSO and then added into the GOX solution. After 8 h of incubation at 4 $^\circ\text{C}$, the reaction product was purified using a desalting column. Different S-TEG-Br to GOX molar ratios from 1.5:1 to 15:1 were used to prepare the GOX–Br conjugates with various initiator moiety to GOX ratios. The average molecular weights of the conjugates were measured by MALDI-TOF MS (TOF/TOF 5800, Hitachi).

Synthesis of GOX–PDMA. The ATRP catalyst solution of CuCl (1 mg, 7.43 μmol) and 1,1,4,7,10,10-hexamethyltriethylenetetramine (HMTETA) (10 μL) in 1 mL of 10 mM PBS in a Schlenk tube was deoxygenated by sparging with nitrogen for 20 min at 0 $^\circ\text{C}$. A mixture of GOX–Br (2 mg, 0.013 μmol) and DMA (8, 11, or 15 μL , 56, 79, or 97 μmol respectively) in 1.5 mL of 10 mM PBS in a Schlenk tube was deoxygenated by sparging with nitrogen for 20 min at 0 $^\circ\text{C}$. Then, the $\text{CuCl}/\text{HMTETA}$ stock solution (500 μL) was transferred into the GOX–Br/DMA mixture (1.5 mL) under the nitrogen protection. The Schlenk tube was sealed and kept at 4 $^\circ\text{C}$. After 4 h of reaction with magnetic stirring, the reaction was stopped by exposing the polymerization solution to air. GOX–PDMA was purified using an AKTA purifier with an anion-exchange column (Bio-Rad) and desalting column (Bio-Rad). GOX, GOX–Br, and purified GOX–PDMA were analyzed by sodium dodecyl-sulfate polyacrylamide gel electrophoresis (SDS-PAGE) and gel permeation chromatography (GPC) systems equipped with a UV–vis detector (Agilent Technologies) and a size exclusion column (PL aquagel-OH MIXED-M 8 μm 300 \times 7.5 mm).

To determine the chemical structure of PDMA of GOX–PDMA, GOX–PDMA was desalted by an AKTA purifier with a desalting column and then lyophilized. 10 mg lyophilized GOX–PDMA was dissolved in D_2O (600 μL) for ^1H NMR measurement on a WNMN-1 400 MHz spectrometer.

To determine the molecular weight and dispersity of PDMA of GOX–PDMA, GOX–PDMA (0.01 nmol) was incubated with proteinase K (3.4 nmol) in 1 mL PBS at 37 $^\circ\text{C}$ for 48 h to digest GOX of the conjugate. The resulting polymer PDMA was analyzed by the GPC system equipped with a refractive index detector and a size exclusion column (Asahipak, GS-520HQ) calibrated with PEG standards.

Synthesis of GOX–PDMA– Fe^0 . A mixture of GOX–PDMA (0.1 μmol) and ammonium iron(II) sulfate (12.6 μmol) in 10 mL PBS was deoxygenated by bubbling with nitrogen for 30 min under stirring. Then, 2 mL of NaBH_4 (29.7 μmol) in cold deionized water was dropwise added to the mixture solution. After 2 h, the product was purified by dialysis against deoxygenated PBS at 4 $^\circ\text{C}$ (MWCO: 30 kD). The morphology of GOX–PDMA– Fe^0 was observed by biological transmission electron microscopy (TEM) (FEI Tecnai Spirit). TEM elemental mapping of GOX–PDMA– Fe^0 was obtained on a FEI Talos F200S. Dynamic light scattering (DLS) measurements were performed on a Microtrac Nanotrak Wave II. ζ potentials of samples at pH 7.4 were measured with a Malvern Zetasizer Nano ZS90 at room temperature. CD spectra of the samples at 0.5 mg/mL in PBS were recorded in the far-UV region (200–250 nm) on a J-1500 (JASCO) instrument.

Synthesis of Fluorophore-Labeled GOX, GOX–PDMA, and GOX–PDMA– Fe^0 . Cy7-labeled GOX, GOX–PDMA, or GOX–PDMA– Fe^0 were prepared by adding Sulfo-Cy7 NHS into a PBS solution (pH 9.0) of GOX, GOX–PDMA, or GOX–PDMA– Fe^0 at a Sulfo-Cy7 NHS to GOX molar ratio of 5, followed by incubation at 4 $^\circ\text{C}$. After 12 h, the product was purified by dialysis against PBS at 4 $^\circ\text{C}$ (MWCO: 30 kD). Notably, Cy7-GOX–PDMA– Fe^0 was prepared under nitrogen protection, and the product was dialyzed in deoxygenated PBS at 4 $^\circ\text{C}$. Similarly, FITC-labeled GOX, GOX–PDMA, and GOX–PDMA– Fe^0 were prepared using the same procedure.

Assay for the Stability of GOX and Its Analogues. To study the stability of GOX and its analogues, the samples (1×10^{-3} mg/mL) were incubated with proteinase K (0.6 mg/mL) at 37 $^\circ\text{C}$ or without proteinase K at 60 $^\circ\text{C}$. At different time intervals, the relative activity of each sample was measured as described in our previously published work.²⁷

Assay for the pH-Responsive Ferrous Ion Release. Ferrous ion release experiment was conducted in the plastic centrifuge tubes with gentle stirring. Each tube contained 10 mL of PBS (10 mM) with a distinct pH value (7.4, 6.5 or 5.4) and a sealed dialysis bag (MWCO 3000 Da) with 1 mL of GOX–PDMA– Fe^0 (0.08 μmol GOX) in PBS. 200 μL of the solution was collected from the tube at different time intervals for the determination of concentration of the released Fe^2+ ions by ICP–MS (Elan DRCII, PerkinElmer).

Assay for the pH and Oxygen Concentration Changes in Cascade Biocatalysis. GOX–PDMA– Fe^0 (2 mg GOX) was added into 20 mL of PBS solutions with varying glucose concentrations (100, 50, and 10 mg/mL). The pH values of the GOX–PDMA– Fe^0 solutions were monitored using a pH meter (PB-10, Sartorius). In addition, after GOX–PDMA– Fe^0 (2 mg GOX) was added into 20 mL of a PBS solution with 1 mg/mL glucose, the O_2 concentration in the GOX–PDMA– Fe^0 solution was detected using a dissolved oxygen meter (JPBJ-609A, RITZ).

Assay for $\cdot\text{OH}$ Generation. In a typical process, 0.3 mL of GOX–PDMA– Fe^0 (100 μg GOX/mL) was added into 3 mL of PBS solutions of glucose (2 mM) and BA (2 mM) at pH 5.4, 6.5, and 7.4. The fluorescence spectrum of OHBA was recorded by a microplate reader (Molecular Devices SpectraMax M3) for 40 min. The generation of $\cdot\text{OH}$ was further detected by electron spin resonance (ESR) spectroscopy. 0.3 mL of GOX–PDMA– Fe^0 (100 μg GOX/mL) was added into 3 mL of PBS solutions of glucose (2 mM) at pH 5.4, 6.5, and 7.4. After 20 min, 30 μL of 5,5-dimethyl-1-pyrroline-*N*-oxide was added to 30 μL of the mixture solution. The resulting solution was tested by ESR (Bruker EMXPLUS) immediately.

Cell Culture. 4T1 cells used in the experiments were treated with RPMI 1640 containing 10% FBS and 1% 100 U/mL penicillin/streptomycin at 37 $^\circ\text{C}$ in a humidified atmosphere with 5% CO_2 .

Cell Viability. The cell viability of PDMA, GOX, GOX–PDMA, or GOX–PDMA– Fe^0 was measured using a methyl thiazolyl tetrazolium (MTT) assay. 4T1 cells were cultured in 96-well plates (5×10^3 cells/well). After 24 h, the cells were divided into five groups: control, PDMA, GOX, GOX–PDMA, and GOX–PDMA– Fe^0 groups. Samples with serial concentrations (20, 40, 60, 80, and 100 ng GOX/mL) were dissolved in the RPMI 1640 medium without

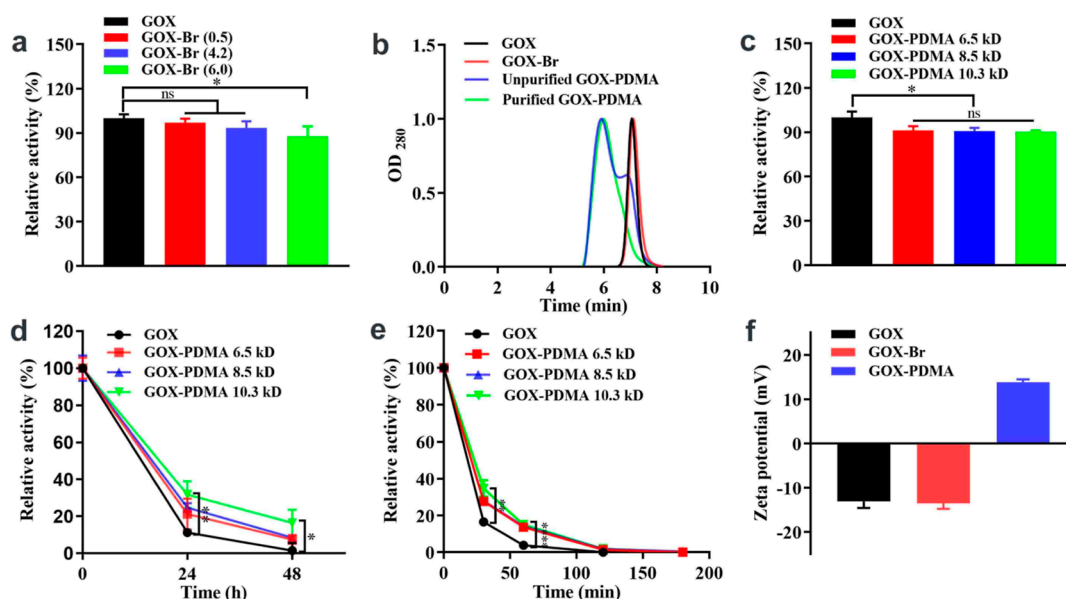


Figure 2. Physicochemical characterization of GOX–PDMA. (a) Relative activity of GOX–Br with different molar ratios of initiating moiety to GOX as compared to GOX ($n = 3$). (b) GPC traces of GOX, GOX–Br, unpurified GOX–PDMA, and purified GOX–PDMA. (c) Relative activity of GOX–PDMA with different molecular weights as compared to GOX ($n = 3$). (d) Relative activity of GOX–PDMA with varying molecular weights after incubation for 24 and 48 h at 60 °C ($n = 3$). (e) Relative activity of GOX–PDMA with varying molecular weights as a function of time after incubation with proteinase K at 37 °C ($n = 3$). (f) ζ potentials of GOX, GOX–Br, and GOX–PDMA at pH 7.4 ($n = 3$).

glucose and 100 μL of the samples added into 96-well plates. After 3 h of incubation, the medium in 96-well culture plates was replaced with the RPMI 1640 medium with FBS and then 10 μL of MTT stock solution (5 mg/mL) was put into each well. After 4 h incubation at 37 °C, the medium was substituted with DMSO (100 μL /well), and the absorbance at 570 nm was recorded.

Endocytic Uptake. 4T1 cells (5×10^5 cells/dish) were cultured in confocal dishes for 24 h. Subsequently, the RPMI 1640 medium was substituted with a glucose-free medium containing PBS, FITC-GOX (3 μg GOX/mL), FITC-GOX–PDMA (3 μg GOX/mL), or FITC-GOX–PDMA–Fe⁰ (3 μg GOX/mL). After 3 h incubation, the 4T1 cells were incubated with Hoechst 33342 (nucleus dye) and DiD (membrane dye), followed by PBS washing. Finally, the cells were imaged by confocal microscopy (LSM900, Carl Zeiss).

4T1 cells were cultured in six-well plates (5×10^5 cells/well) for 24 h, and then the medium was exchanged with a glucose-free medium containing PBS, FITC-GOX (3 μg GOX/mL), FITC-GOX–PDMA (3 μg GOX/mL), or FITC-GOX–PDMA–Fe⁰ (3 μg GOX/mL). After 3 h of incubation, the cells were digested and tested by flow cytometry (CytoFLEX S, Beckman).

Intracellular ROS Production. In a typical process, 4T1 cells (5×10^5 cells/dish) were cultured in confocal dishes for 24 h. Then, 4T1 cells were treated with PBS, GOX (3 μg GOX/mL), GOX–PDMA (3 μg GOX/mL), or GOX–PDMA–Fe⁰ (3 μg GOX/mL) in a glucose-free medium for 3 h. After being washed with PBS three times, the 4T1 cells were incubated with DCFH-DA (10 μM) in RPMI 1640 medium. After 30 min of incubation, the cells were analyzed by confocal microscopy and flow cytometry.

Animal Models. Six to eight week-old female BALB/c mice used in the in vivo experiments (LA2020340) were purchased from the Department of Laboratory Animal Science, Peking University Health Science Center. 4T1 tumor models were prepared by subcutaneously injecting 50 μL stock PBS solution containing 4T1 cells into the back of mice.

In Vivo and Ex Vivo Fluorescence Imaging. 4T1 tumor (120 mm³)-bearing female mice were intratumorally injected with 20 μL of Cy7-labeled GOX-based samples in PBS (700 nM). The IVIS spectrum imaging system was used for fluorescence imaging of the mice at different time intervals. After 24 h, 4T1 bearing mice were

euthanized, and the tumors and main organs were harvested for ex vivo fluorescence imaging.

Maximum Tolerated Dose. 4T1 tumor (120 mm³)-bearing female mice were randomly grouped ($n = 3$), and each group was intratumorally injected with of GOX–PDMA–Fe (5, 4, and 3 mg GOX/kg), GOX–PDMA (4, 3, and 2 mg GOX/kg), or GOX (2.4, 1.6, and 0.8 mg GOX/kg) every 2 days five times. Body weights of the 4T1 tumor-bearing female mice were recorded every 2 days within 12 days. Maximum tolerated dose (MTD) was determined as the maximum concentration of a GOX-based sample that does not lead to over 10% weight loss or significant macroscopic damage.

In Vivo Antitumor Efficacy. To evaluate the antitumor efficacy in vivo, 4T1 cells (1×10^7) were injected subcutaneously into the back region of BALB/c female mice. While the tumor size reached about 120 mm³, the mice were divided randomly into five groups ($n = 6$) and intratumorally injected with different samples: 1, PBS; 2, PDMA (3.8 mg/kg); 3, GOX (0.8 mg GOX/kg); 4, GOX–PDMA (3 mg GOX/kg); and 5, GOX–PDMA–Fe (4 mg GOX/kg) every 2 days five times. The tumor sizes of animals and their body weights were monitored every 2 days.

Histology. 4T1 tumor (120 mm³)-bearing BALB/c mice were intratumorally injected with different samples: 1, PBS; 2, PDMA (3.8 mg/kg); 3, GOX (0.8 mg GOX/kg); 4, GOX–PDMA (3 mg GOX/kg); and 5, GOX–PDMA–Fe (4 mg GOX/kg) every 2 days five times. On day 12, the mice were euthanized, and then the spleen, liver, lung, kidney, and heart were harvested for H&E staining.

Immunohistochemistry. 4T1 tumor (70 mm³)-bearing BALB/c mice were intratumorally injected with different samples: 1, PBS; 2, PDMA (3.8 mg/kg); 3, GOX (0.8 mg GOX/kg); 4, GOX–PDMA (3 mg GOX/kg); and 5, GOX–PDMA–Fe⁰ (4 mg GOX/kg). After 8 h, the mice were euthanized to collect the tumors. The immunohistochemistry tests were conducted using standard laboratory procedures. For CRT evaluation, the samples were treated with rabbit anti-mouse-CRT primary antibody (1:200 dilution). For GRP78 evaluation, the samples were treated with anti-mouse-GRP78 primary antibody (1:300 dilution).

In Vivo Antitumor Immunity. To construct the bilateral tumor model, 4T1 cells (1×10^6) were subcutaneously injected into the left flank of each Balb/c female mouse (primary tumors), and 4T1 cells (5×10^5) were subcutaneously injected into the right flank of each Balb/c

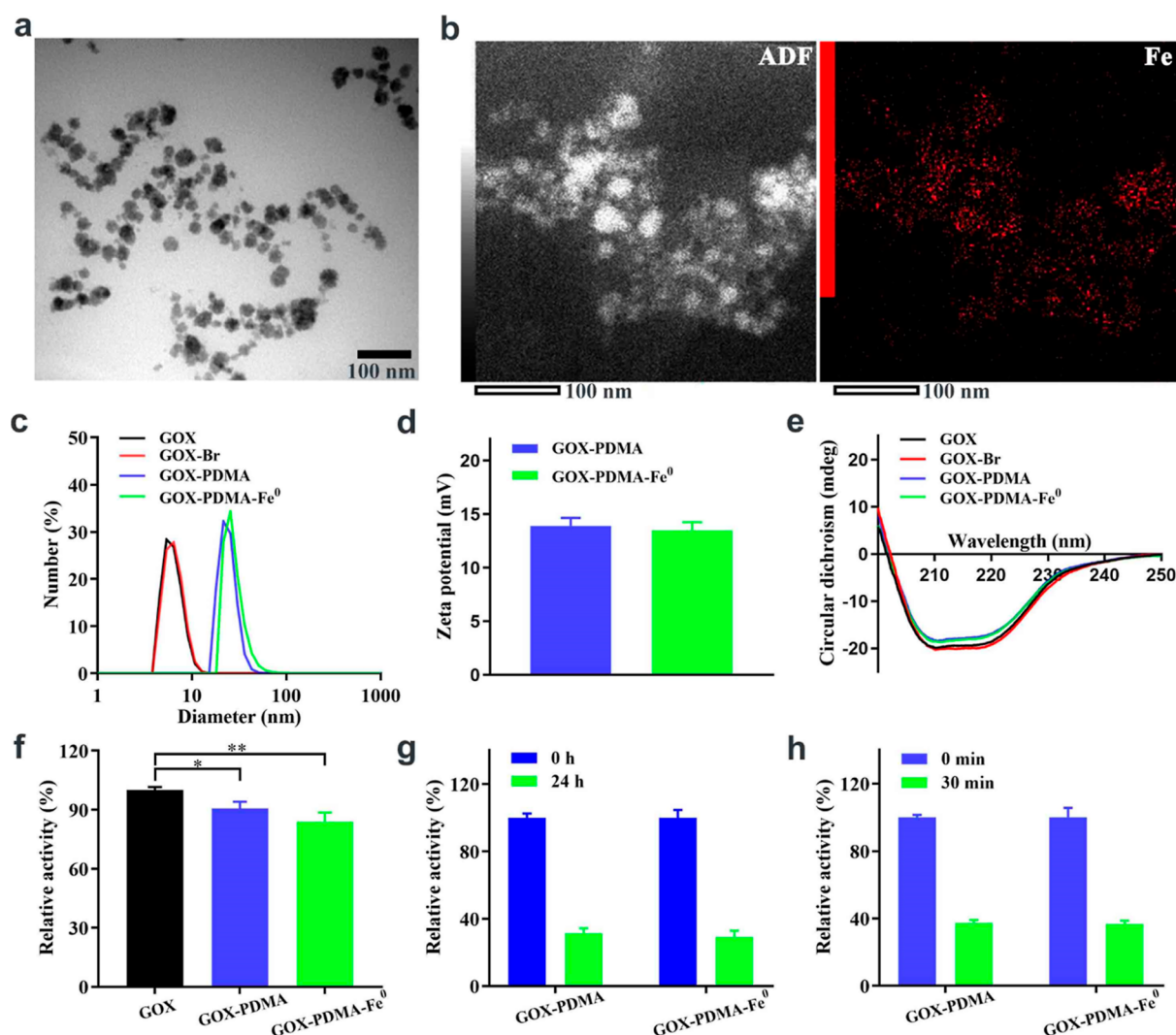


Figure 3. Physicochemical characterization of GOX-PDMA-Fe⁰. (a) Biological TEM image of GOX-PDMA-Fe⁰. (b) Annular dark-field (ADF) TEM image (left panel) and elemental mapping image of GOX-PDMA-Fe⁰ (right panel). (c) DLS analysis. (d) ζ potentials at pH 7.4 ($n = 3$). (e) CD spectra. (f) Relative activity of GOX-PDMA-Fe⁰ and GOX-PDMA as compared to GOX ($n = 3$). (g) Relative activity of GOX-PDMA and GOX-PDMA-Fe⁰ after incubation with proteinase K for 24 h at 37 °C ($n = 3$). (h) Relative activity of GOX-PDMA and GOX-PDMA-Fe⁰ after incubation for 30 min at 60 °C ($n = 3$).

c female mouse (distant tumors). While the primary tumor size reached around 70 mm³, 4T1 tumor-bearing BALB/c mice were divided randomly into four groups: (1) PBS; (2) surgery + aPD-1 (5 mg/kg); (3) GOX-PDMA-Fe (4 mg GOX/kg); and (4) GOX-PDMA-Fe⁰ (4 mg GOX/kg) + aPD-1 (5 mg/kg). Mice were intratumorally injected with PBS or GOX-PDMA-Fe⁰ at 0 and 2 days or surgery at 0 day, and intravenously injected with aPD-1 at 1, 3, and 5 days. To analyze antitumor immune responses, the mice were sacrificed at 16 days. The tumors were collected and mashed to obtain single-cell suspensions. Spleens were also collected and mashed, and red blood cells were removed via a mouse spleen lymphocyte separation kit (Solarbio). The obtained cell suspensions were labeled with PE-anti-mouse CD8 and APC-anti-mouse CD3 to identify the cytotoxic T lymphocytes. After that, the mixtures were analyzed by flow cytometry.

To analyze cytokines in sera and dendritic cells in spleens, the mice were euthanized at 7 days. The sera of the mice were obtained from orbital sinus blood, and the levels of IFN- γ and TNF- α in sera were measured by ELISA kits (Elabscience). Spleens were also collected and mashed, and red blood cells were removed via a mouse spleen lymphocyte separation kit. The collected cell suspensions were labeled with PE-anti-mouse CD86 and APC-anti-mouse CD80 to identify dendritic cell maturation and then analyzed by flow cytometry.

Statistical Analysis. All experimental data are demonstrated as the mean \pm standard deviation (SD). Student *t*-test standard was used for data analysis. * $P < 0.05$, ** $P < 0.01$, and *** $P < 0.001$. All statistical analyses were performed using GraphPad Prism 5 software and Origin 8 software.

RESULTS AND DISCUSSION

Synthesis and Physicochemical Characterization of GOX-PDMA. To synthesize GOX-PDMA, GOX was treated with an *N*-hydroxysuccinimide-activated atom-transfer radical polymerization (ATRP) initiator (S-TEG-Br) to form GOX-ATRP initiator conjugates (GOX-Br). The average molecular weight of GOX-Br was determined by matrix-assisted laser desorption ionization time-of-flight mass spectrometry (MALDI-TOF-MS) (Figure S1). The molar ratio of ATRP initiator to GOX (Br/GOX) was found positively correlated with the feeding molar ratio of S-TEG-Br to GOX. The enzymatic activity of GOX-Br slightly decreased with increasing Br/GOX ratio (Figure 2a). Here, we chose the GOX-Br conjugate with a Br/GOX molar ratio of 4.2 for the following ATRP reactions considering the high activity

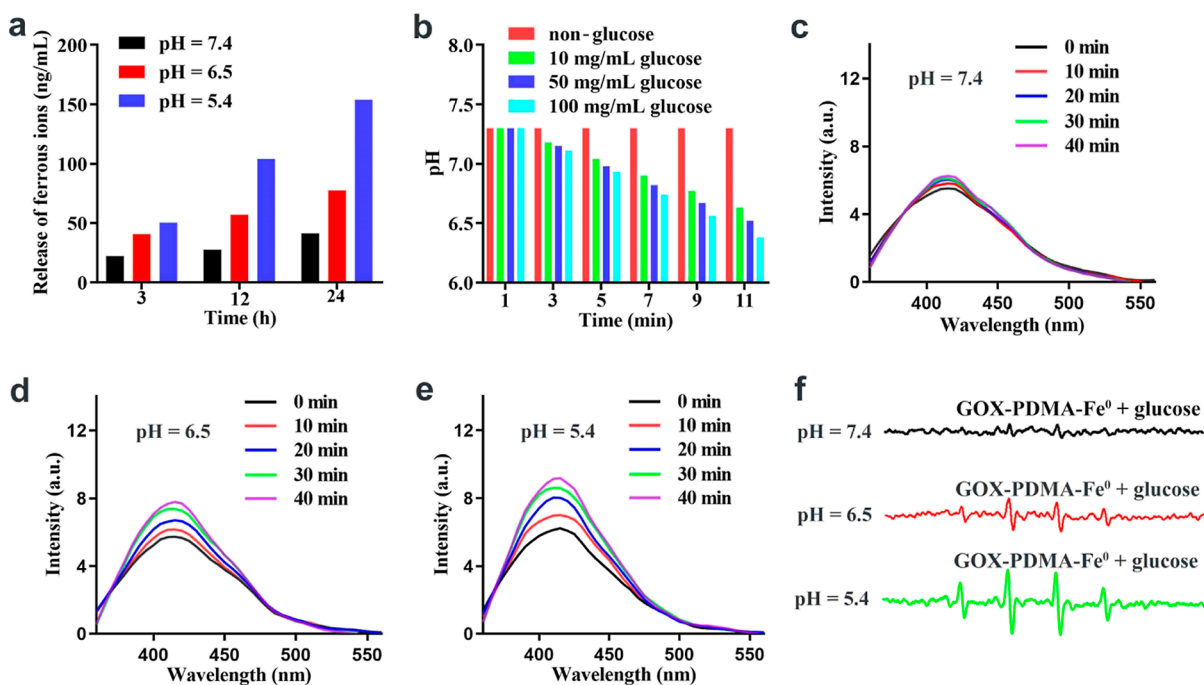


Figure 4. Self-activated cascade biocatalysis of GOX-PDMA-Fe⁰. (a) Release of iron ions from GOX-PDMA-Fe⁰ at different pH values. (b) The time dependence of pH of the solution of GOX-PDMA-Fe⁰ at varying concentrations of glucose. (c–e) Evolutions of the fluorescence spectra for OHBA formed by adding glucose and BA into GOX-PDMA-Fe⁰ solutions at varying pH values of 7.4, 6.5, and 5.4. (f) ESR spectra of GOX-PDMA-Fe⁰ plus glucose at pH 7.4, 6.5, and 5.4.

retention at this ratio. After the ATRP of DMA using the GOX-Br as the initiator in a water-ice bath for 4 h, the solution was directly analyzed by GPC (Figure 2b). Representatively, a new GPC peak for a GOX-PDMA conjugate appeared at a lower elution time than for GOX-Br, while the GPC peak area for GOX-Br diminished significantly, indicating the formation of a GOX-PDMA conjugate with a higher molecular weight than for GOX-Br. The ATRP solution was further purified by anion exchange chromatography to obtain the purified GOX-PDMA conjugate, as indicated by the single GPC peak for the conjugate without the presence of the GPC peak for GOX-Br. The result was confirmed by SDS-PAGE (Figure S2). The chemical structure of PDMA of the conjugate was identified by proton nuclear magnetic resonance (¹H NMR) (Figure S3). The molecular weights of PDMA of the conjugates were adjusted by tuning the feeding molar ratio of DMA to GOX-Br, which were measured by GPC to be 6.5 kD (dispersity = 1.38), 8.5 kD (dispersity = 1.41), and 10.3 kD (dispersity = 1.45), respectively (Figure S4). The enzymatic activity of the conjugates was found to be as high as 90% of that of GOX and independent of the molecular weight of the PDMA (Figure 2c), indicating that the in situ ATRP reactions scarcely affect the activity of GOX. The thermal and proteolytic stabilities of the conjugates are positively correlated to the molecular weight of the PDMA due to the physical shielding of the PDMA on GOX, as indicated by the slower decrease of activity for the conjugate with the higher molecular weight (Figure 2d,e). The ζ potential of GOX-PDMA was positive due to the protonated state of the PDMA, in contrast to the negative ζ potentials of GOX-Br and GOX (Figure 2f). On the basis of these results, we chose the conjugate with a high molecular weight of 10.3 kD for the in situ synthesis of GOX-PDMA-Fe⁰ nanoconjugates.

Synthesis and Physicochemical Characterization of GOX-PDMA-Fe⁰. To prepare GOX-PDMA-Fe⁰ nanoconjugates, the GOX-PDMA conjugate was complexed with ammonium ferrous sulfate due to the iron-nitrogen coordination, followed by the in situ reduction of Fe²⁺ with sodium borohydride into Fe⁰. The morphology of GOX-PDMA-Fe⁰ was observed by biological TEM, and elemental distribution of GOX-PDMA-Fe⁰ was further analyzed by TEM. The average size of the nanoconjugates was determined by biological TEM to be 21 nm in diameter (Figure 3a). Elemental mapping revealed that Fe⁰ nanoparticles were evenly distributed on the nanoconjugates (Figure 3b), indicating the success in the in situ synthesis of GOX-PDMA-Fe⁰ using GOX-PDMA as a template. Electron diffraction indicated the amorphous state of the Fe⁰ nanoparticles (Figure S5). The hydrodynamic radius of the nanoconjugate was measured by DLS to be 27.7 nm. Specifically, the size was 1.2-, 4.1-, and 4.2-fold larger than those of GOX-PDMA (23.9 nm), GOX-Br (6.8 nm), and GOX (6.6 nm), respectively (Figure 3c). The ζ potential of GOX-PDMA-Fe⁰ was positive, which was similar to that of the GOX-PDMA (Figure 3d), indicating the in situ formation of Fe⁰ nanoparticles on GOX-PDMA does not change the overall electric potential of GOX-PDMA significantly. Circular dichroism (CD) demonstrated that the secondary structures of GOX-PDMA-Fe⁰, GOX-PDMA, and GOX-Br were similar to that of GOX (Figure 3e). The enzymatic activities of GOX-PDMA-Fe⁰ and GOX-PDMA were 84.0 and 90.7% of that of native GOX, respectively (Figure 3f). The thermal and proteolytic stabilities of GOX-PDMA-Fe⁰ were similar to those of GOX-PDMA (Figure 3g,h). These results indicate that the in situ formation of Fe⁰ nanoparticles on GOX-PDMA hardly damages the structure, activity, and the stability of GOX.

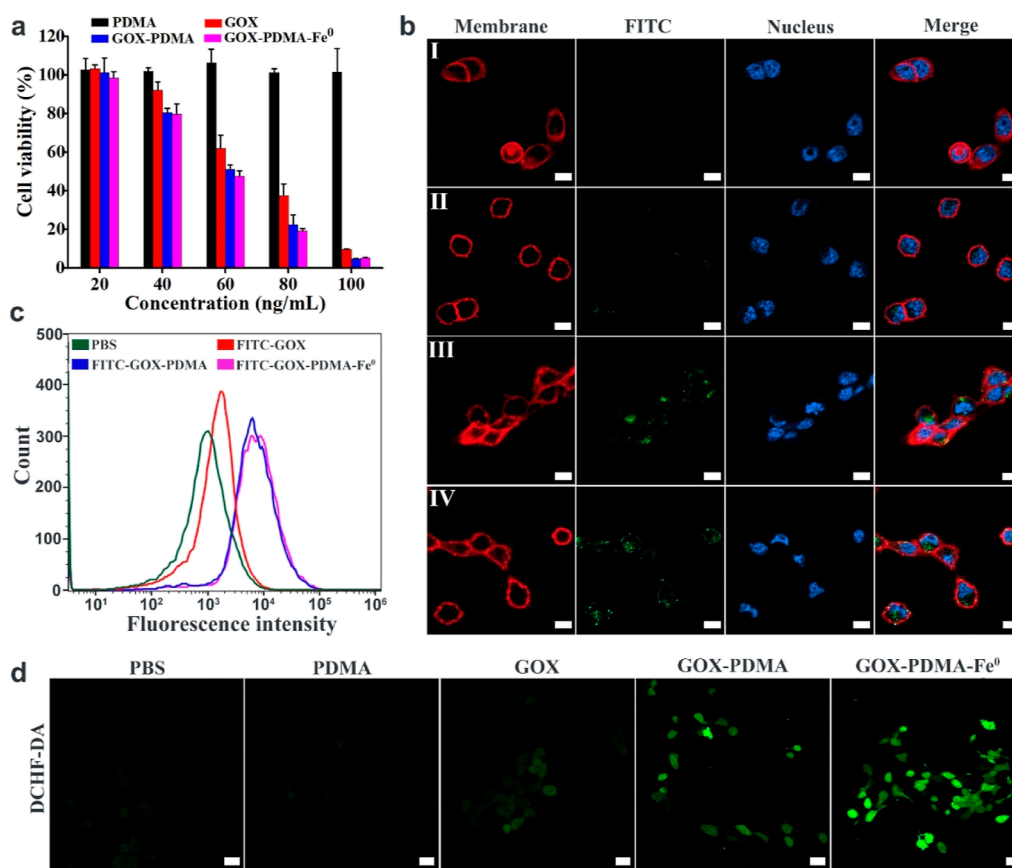


Figure 5. In vitro biological effects of GOX–PDMA–Fe⁰. (a) 4T1 cell viability after varying treatments for 3 h ($n = 4$). (b,c) CLSM and flow cytometry of 4T1 cells after different treatments for 3 h (scale bars = 10 μm). I: PBS, II: FITC-GOX, III: FITC-GOX–PDMA, and IV: FITC-GOX–PDMA–Fe⁰. Green, red, and blue represent GOX analogues, cell membrane, and cell nucleus, respectively. (d) CLSM of the ROS generation in 4T1 cells after different treatments for 3 h (scale bars = 20 μm).

Self-Activated Cascade Biocatalysis of GOX–PDMA–Fe⁰. The performance of cascade biocatalysis of GOX–PDMA–Fe⁰ was evaluated. At first, we studied the release profiles of Fe ions from GOX–PDMA–Fe⁰ at various pH values (Figure 4a). The release rate of Fe ions increased with the decrease in the pH value, indicating that this release can be accelerated in acidic environments. Upon the addition of glucose, the pH values of the solutions of GOX–PDMA–Fe⁰ dropped with the increase in incubation time and glucose concentration (Figure 4b). Meanwhile, the O₂ concentration of the GOX–PDMA–Fe⁰ solution rapidly decreased from 7.86 to 0.77 mg/L in 570 s (Figure S6). These results demonstrate that GOX–PDMA–Fe⁰ can convert glucose into gluconic acid and O₂ into H₂O₂. The potential of GOX–PDMA–Fe⁰ as a self-activated cascade nanobiocatalyst for the generation of [•]OH was investigated by the benzoic acid (BA) assay in which BA was oxidized by [•]OH for the formation of a fluorophore isomeric hydroxybenzoic acid (OHBA) (Figure 4c–e). The OHBA fluorescence intensity increased with the increase in incubation time and the decrease in the starting pH value of the GOX–PDMA–Fe⁰ solution, suggesting the generation of more [•]OH, due to the increased release of Fe²⁺ and thereafter, the acceleration of the Fenton reaction in acidic environments. The ESR signal intensity increased with the decrease in the starting pH value of the GOX–PDMA–Fe⁰ solution (Figure 4f), which further verifies the pH dependence of the [•]OH generation. Together, these results demonstrate that the self-

activated cascade biocatalysis of GOX–PDMA–Fe⁰ leads to the efficient production of [•]OH.

In Vitro Biological Effects of GOX–PDMA–Fe⁰. On the basis of the physicochemical properties, we studied the cytotoxicity of GOX–PDMA–Fe⁰ by using a triple-negative breast cancer cell line 4T1 (Figure 5a). The half-maximal inhibitory concentration (IC₅₀) of GOX–PDMA–Fe⁰ was determined to be 62.1 ng GOX/mL, which was 1.2- and 1.5-fold lower than those of GOX–PDMA (77.0 ng GOX/mL) and GOX (93.0 ng GOX/mL), respectively, indicating that GOX–PDMA–Fe⁰ is more cytotoxic than GOX–PDMA and GOX. In contrast, PDMA was found to be non-toxic to 4T1 cells in the experiments. The endocytosis of GOX–PDMA–Fe⁰ was further examined after labeling it with FITC. Confocal laser scanning microscopy (CLSM) exhibited that the green fluorescence intensity in the 4T1 cells incubated with the FITC-labeled GOX–PDMA–Fe⁰ or GOX–PDMA was much stronger than that in the 4T1 cells treated with the FITC-labeled GOX (Figure 5b). This result was supported by flow cytometry (Figure 5c). The fluorescence intensity of the FITC-labeled GOX–PDMA–Fe⁰ or GOX–PDMA-treated 4T1 cells was 9.2 or 9.4 folds greater than that of the FITC-labeled GOX, respectively (Figure S7). These data indicate the similarity of GOX–PDMA–Fe⁰ to GOX–PDMA and the superiority of GOX–PDMA–Fe⁰ over GOX in endocytosis, due to the electrostatic interaction between GOX–PDMA–Fe⁰ or GOX–PDMA and 4T1 cells. Next, we used 2',7'-dichlorofluorescein diacetate (DCFH-DA) as a ROS fluo-

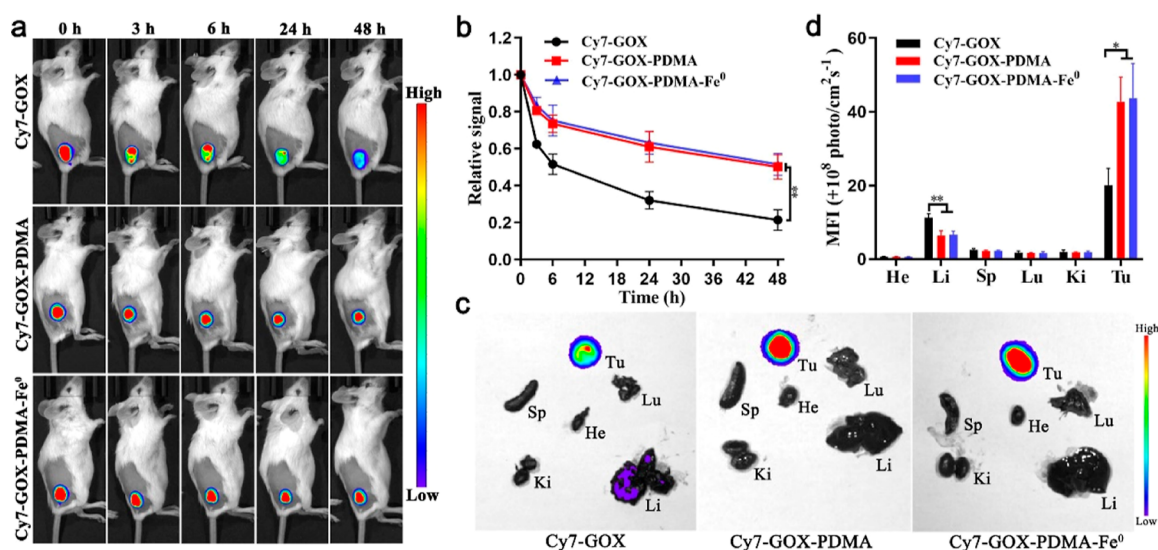


Figure 6. Tumor retention and biodistribution of GOX–PDMA–Fe⁰ after intratumoral injection. (a) Fluorescence imaging of 4T1-bearing mice after a single intratumoral injection of Cy7-GOX, Cy7-GOX–PDMA, or Cy7-GOX–PDMA–Fe⁰. (b) Relative fluorescence–time curves of the 4T1 tumors treated with Cy7-GOX, Cy7-GOX–PDMA, or Cy7-GOX–PDMA–Fe⁰, quantified from (a) ($n = 3$). (c) Ex vivo imaging of tumor and major organs, including the tumor (Tu), kidney (Ki), liver (Li), lung (Lu), spleen (Sp), and heart (He), at 24 h after a single intratumoral injection with Cy7-GOX, Cy7-GOX–PDMA, or Cy7-GOX–PDMA–Fe⁰. (d) Values of fluorescence intensity of the tumor and major organs, quantified from (c) ($n = 3$). P values: $^{**}P < 0.01$, or $^{*}P < 0.05$.

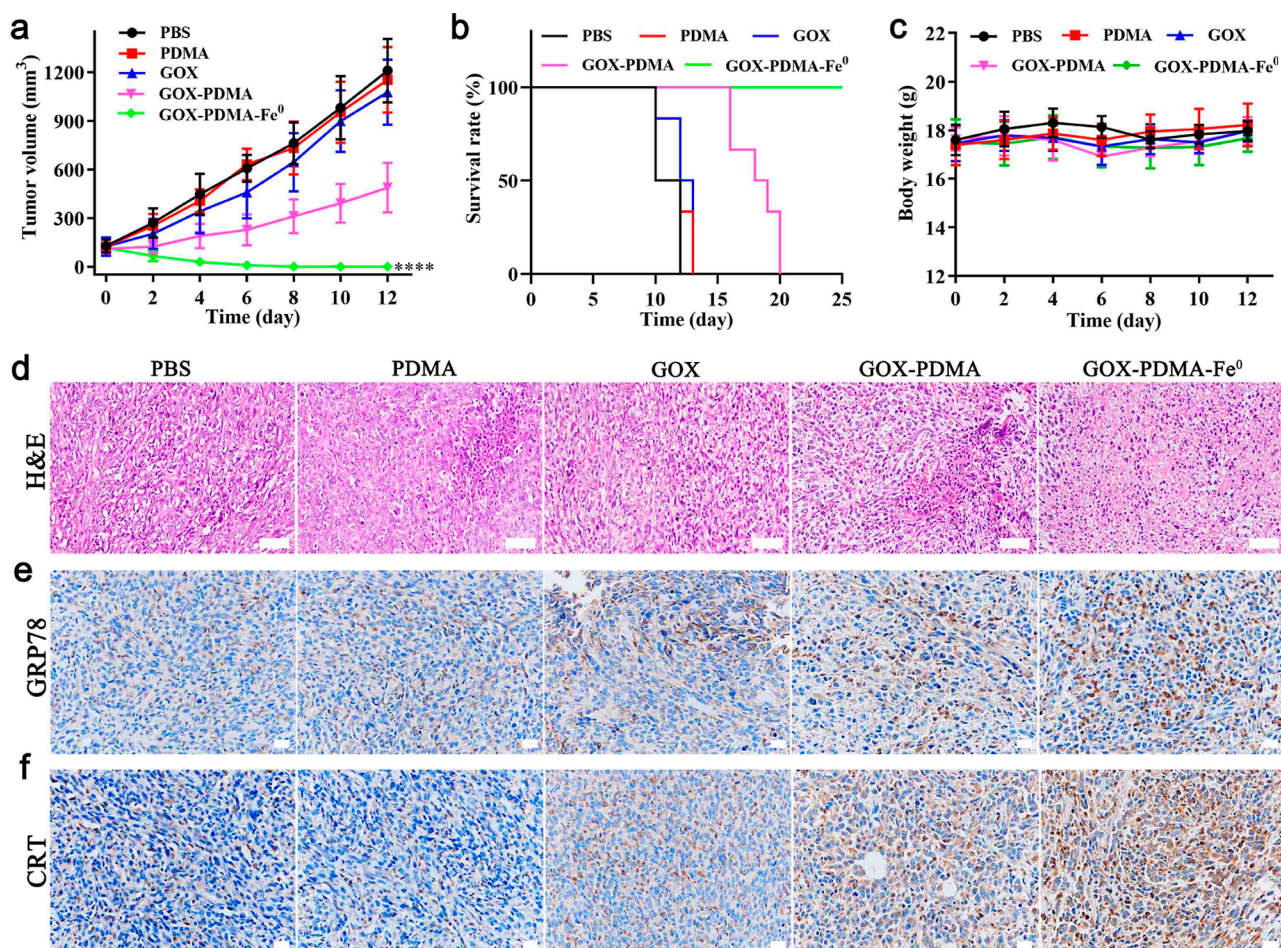


Figure 7. In vivo biological effects of GOX–PDMA–Fe⁰ in mice-bearing 4T1 tumors. (a) Tumor growth curves ($n = 6$). (b) Animal survival curves ($n = 6$). (c) Animal body weight change curves ($n = 6$). (d) H&E staining of tumor tissues (scale bars = 50 μm). (e,f) Immunohistochemistry of GRP78 and CRT in tumor tissues (scale bars = 20 μm). Blue represents the nucleus and brown or tan represents the target protein. P values: $^{****}P < 0.0001$, $^{**}P < 0.01$.

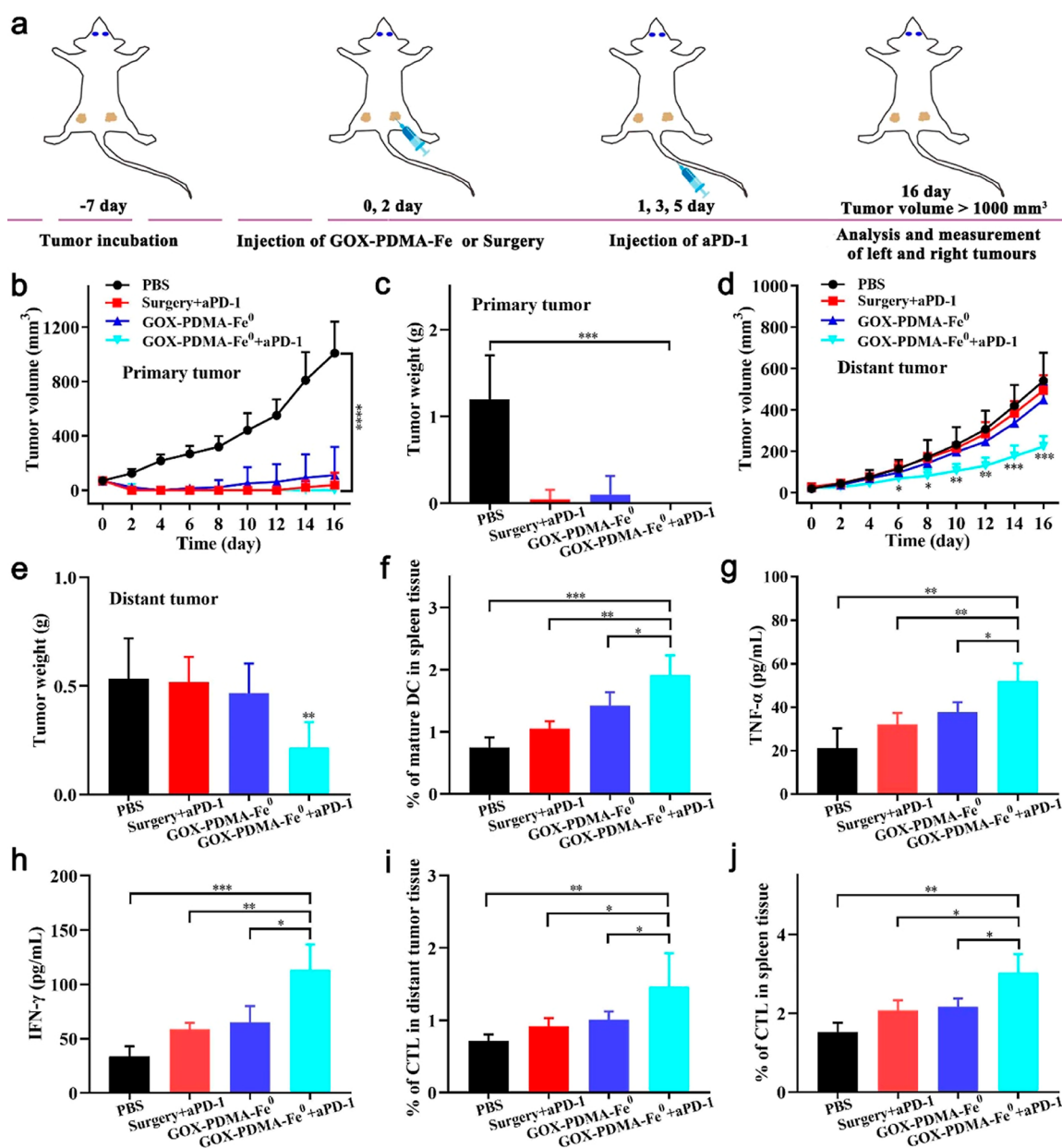


Figure 8. Abscopal effect of GOX–PDMA–Fe⁰ in combination with aPD-1 in cancer immunotherapy. (a) Schematic illustration of combining GOX–PDMA–Fe⁰ with aPD-1 to treat 4T1 tumors in mice. (b) Growth inhibition of the primary tumors ($n = 6$). (c) Average weights of the primary tumors at 16 days ($n = 6$). (d) Growth inhibition of the distant tumors ($n = 6$). (e) Average weights of the distant tumors at 16 days ($n = 6$). (f) Percentages of mature DCs in splenocytes of the mice treated with PBS, surgery + aPD-1, GOX–PDMA–Fe⁰, or GOX–PDMA–Fe⁰ + aPD-1. (g,h) TNF- α and IFN- γ levels in sera from the 4T1 tumor-bearing mice at 7 days ($n = 4$). (i,j) Percentage of CTLs in the tumor and spleen tissues at 16 days ($n = 4$). P values: **** $P < 0.0001$, *** $P < 0.001$, ** $P < 0.01$, or * $P < 0.05$.

rescent probe to detect the intracellular ROS. The green fluorescence in the GOX–PDMA–Fe⁰-treated 4T1 cells was greater than in the GOX–PDMA-treated or GOX-treated 4T1 cells (Figure 5d), which was verified by flow cytometry, in which the fluorescence intensity of the GOX–PDMA–Fe⁰-treated 4T1 cells was 1.25- and 1.87-fold higher than those of the GOX–PDMA-treated and GOX-treated 4T1 cells, respectively (Figure S8). These data indicate that GOX–PDMA–Fe⁰ and GOX–PDMA induce more intracellular ROS than GOX due to the enhanced endocytosis. GOX–PDMA–Fe⁰ induced more intracellular ROS than GOX–PDMA due to the generation of more cytotoxic $\cdot\text{OH}$ than H_2O_2 via the self-activated cascade biocatalysis in the 4T1 cells. Taken together, these results show the enhanced cytotoxicity of GOX–

PDMA–Fe⁰ over GOX–PDMA and GOX, owing to the self-activated cascade biocatalysis or/and the enhanced endocytosis.

Tumor Retention and Biodistribution of GOX–PDMA–Fe⁰. We evaluated the MTD of GOX–PDMA–Fe⁰ after intratumoral injection in mice bearing 4T1 tumors (Figure S9). The MTD of GOX–PDMA–Fe⁰ was determined to be 4 mg GOX/kg body weight, which was 1.3 and 5.0-fold greater than those of GOX–PDMA (3 mg GOX/kg body weight) and GOX (0.8 mg GOX/kg body weight), respectively. These data indicate that GOX–PDMA–Fe⁰ and GOX–PDMA are more tolerable than GOX, which might be ascribed to the enhanced tumor retention caused by not only the enlarged size and increased stability of GOX–PDMA–Fe⁰

or GOX–PDMA over GOX but also the electrostatic interaction between GOX–PDMA–Fe⁰ or GOX–PDMA and tumor cells. To prove the hypothesis, GOX–PDMA–Fe⁰ and GOX–PDMA were labeled with Cyanine7 (Cy7) for the investigation of the tumor retention after intratumoral injection (Figure 6a). The fluorescence intensity in the tumors injected with Cy7-GOX–PDMA–Fe⁰ and Cy7-GOX–PDMA diminished with the time much more slowly than in the tumors treated with Cy7-GOX (Figure 6b). Specifically, the fluorescence intensities in the tumors injected with Cy7-GOX–PDMA–Fe⁰ and Cy7-GOX–PDMA were 2.3- and 2.4-folds greater than in the tumors injected with Cy7-GOX at 24 h, respectively. These data indicate the considerably increased tumor retention of GOX–PDMA–Fe⁰ and GOX–PDMA than GOX. Next, we sacrificed the mice at 24 h and harvested the tumor and main organs for ex vivo imaging (Figure 6c). Notably, the fluorescence intensities of the tumors injected with Cy7-GOX–PDMA–Fe⁰ and Cy7-GOX–PDMA were 2.2- and 2.1-fold greater than of the tumors injected with Cy7-GOX, respectively (Figure 6d), whereas the fluorescence intensities of the livers in the treatment groups of Cy7-GOX–PDMA–Fe⁰ and Cy7-GOX–PDMA were 0.59- and 0.57-fold weaker than in the treatment group of Cy7-GOX, respectively. These results confirm the enhanced tumor retention of GOX–PDMA–Fe⁰ and GOX–PDMA over GOX.

In Vivo Biological Effects of GOX–PDMA–Fe⁰. We studied the antitumor efficacy of GOX–PDMA–Fe⁰, in mice bearing 4T1 tumors, that was intratumorally injected at the MTD on days 0, 2, 4, 6, and 8. GOX–PDMA–Fe⁰ eradicated the tumors, whereas GOX–PDMA could not show the same effect but was superior to GOX in suppressing tumor growth (Figures 7a and S10). As expected, PDMA did not show any antitumor efficacy. The enhanced antitumor efficacy was correlated with the increased animal survival rate (Figure 7b). All of the GOX–PDMA–Fe⁰-treated animals survived without any visible tumor burden. In contrast, the median animal survival times of GOX–PDMA, GOX, PDMA, and PBS were 18, 12, 10, and 10 d, respectively. These results indicate that GOX–PDMA–Fe⁰ outperforms GOX–PDMA and GOX in the treatment of 4T1 tumors. No significant loss of animal body weight and no obvious damage in hematoxylin–eosin (H&E) staining of the kidney, liver, lung, spleen, and heart were observed in all the treatment groups, indicating that all the treatments did not cause severe side effects (Figures 7c and S11).

The antitumor activity of GOX–PDMA–Fe⁰ was verified by H&E staining of the tumor tissue, in which the most serious tumor cell destruction was found in the treatment group of GOX–PDMA–Fe⁰ (Figure 7d). Here, we hypothesized that the highly efficient antitumor efficacy of GOX–PDMA–Fe⁰ would effectively induce the program of ICD. In ICD, endoplasmic reticulum (ER) stress performs a crucial role in immunogen exposure. The upregulation of glucose-regulated protein 78 kD (GRP78) is a specific indication for a ER stress response.^{40,41} In response to ER stress, calreticulin (CRT) migrates from ER lumen onto the surface of the cell to serve as an “eat-me” signal.^{42,43} Indeed, higher levels of GRP78 and CRT proteins were detected in the treatment group of GOX–PDMA–Fe⁰ than in the other groups (Figure 7e,f), indicating that GOX–PDMA–Fe⁰ induces a stronger ER stress response and ICD in vivo than GOX–PDMA, due to the higher cytotoxicity of •OH generated by GOX–PDMA–Fe⁰ than that of H₂O₂ produced by GOX–PDMA and GOX.

Abscopal Effect of GOX–PDMA–Fe⁰ in Combination with aPD-1. aPD-1 is one of the most widely used immune checkpoint inhibitors, which can effectively inhibit PD-1/PDL-1 axis to preclude the tumor immune escape.⁴⁴ Therefore, we chose aPD-1 to synergize with the nanoconjugate for durable and effective immunotherapy. To prove our hypothesis, primary and distant 4T1 tumors were established at the two franks of mice (Figure 8a). The nanoconjugate was injected at the MTD into the primary tumors at 0 and 2 days, or the primary tumors were removed by surgery at 0 day. The antibody was injected at a dosage of 5 mg/kg body weight at 1, 3, and 5 days. GOX–PDMA–Fe⁰ + aPD-1 completely ablated the primary tumors, whereas GOX–PDMA–Fe⁰ alone or surgery + aPD-1 did not show such efficacy (Figures 8b and S12 and S13). At 16 days, the average weights of the primary tumors in the groups of GOX–PDMA–Fe⁰ + aPD-1, GOX–PDMA–Fe⁰, surgery + aPD-1, and PBS were 0, 0.1, 0.3, and 1.2 g, respectively (Figure 8c). The data indicate that the combination of GOX–PDMA–Fe⁰ and aPD-1 generates the synergistic effect in the treatment of 4T1 tumors. Importantly, the growth of the distant tumors was more efficiently inhibited by GOX–PDMA–Fe⁰ + aPD-1 than the other treatments (Figure 8d). On day 16, the average weight of the distant tumors in the group of GOX–PDMA–Fe⁰ aPD-1 (0.22 g) was 2.1-, 2.4-, and 2.4-fold lower than in the groups of GOX–PDMA–Fe⁰ (0.47 g), surgery + aPD-1 (0.52 g), and PBS (0.53 g), respectively (Figure 8e). These results indicate that GOX–PDMA–Fe⁰ + aPD-1 can more efficiently induce the abscopal effect on the tumors than GOX–PDMA–Fe⁰ alone and surgery + aPD-1.

We further investigated the antitumor immunity of GOX–PDMA–Fe⁰ + aPD-1. Dendritic cells (DCs) play an essential role in the initiation, regulation, and adaptation of immunity.⁴⁵ The states of DCs were analyzed after the treatments with PBS, surgery + aPD-1, GOX–PDMA–Fe⁰ alone, and GOX–PDMA–Fe⁰ + aPD-1. The cells in the spleen were harvested for flow cytometry analysis (Figures 8f and S14). The percentages of mature DCs (CD86 and CD80) in the group of GOX–PDMA–Fe⁰ + aPD-1 (1.9%) were 1.4-, 1.8-, and 2.5-fold greater than those in the groups of GOX–PDMA–Fe⁰ (1.4%), surgery + aPD-1 (1.05%), and PBS (0.75%), respectively, indicating that GOX–PDMA–Fe⁰ + aPD-1 is the most efficient in maturing DCs. The serum levels of interferon gamma (IFN-γ) and tumor necrosis factor-alpha (TNF-α) in the GOX–PDMA–Fe⁰ + aPD-1 group were found to be the highest (Figure 8g,h), demonstrating the strongest immune response. Additionally, the distant tumors and spleens were collected and analyzed by flow cytometry (Figures 8i,j and S15 and S16). The percentages of cytotoxic T lymphocytes (CTLs) (CD3 and CD8) from the distant tumors and spleens were the highest in the group of GOX–PDMA–Fe⁰ + aPD-1, indicating the most efficient immune response. Collectively, these results indicate that GOX–PDMA–Fe⁰ + aPD-1 induces the most durable and effective immune response because of the synergistic combination of ICD induced by the nanoconjugate and ICB achieved by aPD-1.

We also evaluated the biosafety of GOX–PDMA–Fe⁰ + aPD-1 in vivo. No severe side effects were observed in all the groups, as indicated by the increase in body weight in all the treatment groups (Figure S17). H&E staining showed that all the treatments did not exhibit obvious damage to the vital organs (Figure S18). These results demonstrate that the

treatment of GOX–PDMA–Fe⁰ + aPD-1 does not cause significant side effects in vivo.

CONCLUSIONS

The in situ growth of PDMA from GOX efficiently yields GOX–PDMA conjugates as a template for the in situ formation of GOX–PDMA–Fe⁰ nanoconjugates with well-retained enzymatic activity. The nanoconjugates catalyze the conversions of glucose into gluconic acid and O₂ into H₂O₂. The accumulative production of gluconic acid lowers the local pH value of the nanoconjugates, which can accelerate the ionization of Fe nanoparticles into Fe²⁺ for the conversion of H₂O₂ into •OH via a Fenton reaction. On the basis of the self-activated cascade biocatalysis, the nanoconjugates can not only block energy (glucose) supply for tumor cell growth and metabolism but also directly kill tumor cells by the generation of highly cytotoxic •OH. Furthermore, the electrostatic interaction between the nanoconjugates and tumor cells facilitates the endocytosis and increases the tumor retention after intratumoral injection, leading to the dramatically enhanced MTD and antitumor efficacy. Due to the advantages, the nanoconjugates efficiently induce ICD in vivo, which stimulates antigen-specific immune responses and reverses the immunosuppressive microenvironment for the enhanced ICB therapy. More importantly, the synergy of the self-activated cascade biocatalysis and ICB therapies leads to the abscopal effect on the tumors. In general, this method should be applicable to other H₂O₂-generating enzymes, such as xanthine oxidase, D-amino acid oxidase, lactate oxidase, and oxalate oxidase, to efficiently generate enzyme-PDMA-Fe⁰ nanoconjugates as self-activated cascade nanobiocatalysts for both cascade biocatalysis therapy and cascade biocatalysis-enhanced immunotherapy of solid tumors.

ASSOCIATED CONTENT

Supporting Information

The Supporting Information is available free of charge at <https://pubs.acs.org/doi/10.1021/acsami.2c04894>.

MALDI-TOF-MS of GOX and GOX–Br, SDS-PAGE analysis and ¹H NMR spectrum of GOX–PDMA, GPC analysis, SAED analysis, and the oxygen concentration change curves of GOX–PDMA–Fe⁰, quantified cellular uptake, flow cytometry analysis of ROS generation, MTD measurements, digital images of 4T1 bearing-tumor mice after different treatments, H&E staining of major tissues, growth curves of primary tumors and distant tumors, flow cytometry analysis of mature DCs and CTLs, and body weight change curves of mice (PDF)

AUTHOR INFORMATION

Corresponding Authors

Xuliang Deng – Department of Geriatric Dentistry, Beijing Laboratory of Biomedical Materials, Peking University School and Hospital of Stomatology, Beijing 100081, China; Biomedical Engineering Department, Peking University, Beijing 100191, China; Peking University-Yunnan Baiyao International Medical Research Center, Beijing 100191, China; Email: kqdengxuliang@bjmu.edu.cn

Weiping Gao – Department of Geriatric Dentistry, Beijing Laboratory of Biomedical Materials, Peking University School and Hospital of Stomatology, Beijing 100081, China;

Biomedical Engineering Department, Peking University, Beijing 100191, China; Peking University International Cancer Institute, Beijing 100191, China; Peking University-Yunnan Baiyao International Medical Research Center, Beijing 100191, China; Institute of Medical Technology, Health Science Center of Peking University, Beijing 100191, China; orcid.org/0000-0002-2916-3044; Email: gaoweiping@hsc.pku.edu.cn

Authors

Fei Duan – Department of Geriatric Dentistry, Beijing Laboratory of Biomedical Materials, Peking University School and Hospital of Stomatology, Beijing 100081, China; Biomedical Engineering Department, Peking University, Beijing 100191, China

Wei Jin – Biomedical Engineering Department, Peking University, Beijing 100191, China

Tong Zhang – Department of Geriatric Dentistry, Beijing Laboratory of Biomedical Materials, Peking University School and Hospital of Stomatology, Beijing 100081, China; Centre for Advanced Macromolecular Design and Australian Centre for NanoMedicine, School of Chemical Engineering, The University of New South Wales, Sydney, New South Wales 2052, Australia

Fan Zhang – Department of Geriatric Dentistry, Beijing Laboratory of Biomedical Materials, Peking University School and Hospital of Stomatology, Beijing 100081, China; Biomedical Engineering Department, Peking University, Beijing 100191, China; Institute of Medical Technology, Health Science Center of Peking University, Beijing 100191, China

Like Gong – Department of Geriatric Dentistry, Beijing Laboratory of Biomedical Materials, Peking University School and Hospital of Stomatology, Beijing 100081, China; Biomedical Engineering Department, Peking University, Beijing 100191, China; Institute of Medical Technology, Health Science Center of Peking University, Beijing 100191, China

Xinyu Liu – Department of Geriatric Dentistry, Beijing Laboratory of Biomedical Materials, Peking University School and Hospital of Stomatology, Beijing 100081, China; Biomedical Engineering Department, Peking University, Beijing 100191, China

Complete contact information is available at: <https://pubs.acs.org/10.1021/acsami.2c04894>

Author Contributions

W.G. conceived and supervised the project with X.D. W.G. wrote the manuscript; W.G. and F.D. analyzed the data; F.D. performed the experiments; W.J. and F.Z. participated in animal experiments; T.Z., L.G. and X.L. revised the paper; and all authors proofread the manuscript.

Notes

The authors declare no competing financial interest.

ACKNOWLEDGMENTS

This work received support from the National Natural Science Foundation of China (81991505 and 21534006).

REFERENCES

(1) Mahoney, K. M.; Rennert, P. D.; Freeman, G. J. Combination Cancer Immunotherapy and New Immunomodulatory Targets. *Nat. Rev. Drug Discovery* **2015**, *14*, 561–584.

- (2) Gotwals, P.; Cameron, S.; Cipolletta, D.; Cremasco, V.; Crystal, A.; Hewes, B.; Mueller, B.; Quarantino, S.; Sabatos-Peyton, C.; Petruzzelli, L.; Engelman, J. A.; Dranoff, G. Prospects for Combining Targeted and Conventional Cancer Therapy with Immunotherapy. *Nat. Rev. Cancer* **2017**, *17*, 286–301.
- (3) Ribas, A.; Wolchok, D. Cancer Immunotherapy Using Checkpoint Blockade. *Science* **2018**, *359*, 1350–1355.
- (4) Routy, B.; Le Chatelier, E. L.; Derosa, L.; Duong, C. P. M.; Alou, M. T.; Daillère, R.; Fluckiger, A.; Messaoudene, M.; Rauber, C.; Roberti, M. P.; Fidelle, M.; Flament, C.; Poirier-Colame, V.; Opolon, P.; Klein, C.; Iribarren, K.; Mondragón, L.; Jacquelot, N.; Qu, B.; Ferrere, G.; Clémenson, C.; Mezquita, L.; Masip, J. R.; Naltet, C.; Brosseau, S.; Kaderbhai, C.; Richard, C.; Rizvi, H.; Levenez, F.; Galleron, N.; Quinquis, B.; Pons, N.; Ryffel, B.; Minard-Colin, V.; Gonin, P.; Soria, J.-C.; Deutsch, E.; Lloriot, Y.; Ghiringhelli, F.; Zalcman, G.; Goldwasser, F.; Escudier, B.; Hellmann, M. D.; Eggermont, A.; Raouf, D.; Albiges, L.; Kroemer, G.; Zitvogel, L. Gut Microbiome Influences Efficacy of PD-1-based Immunotherapy against Epithelial Tumors. *Science* **2018**, *359*, 91–97.
- (5) June, C. H.; O'Connor, R. S.; Kawalekar, O. U.; Ghassemi, S.; Milone, M. C. CAR T Cell Immunotherapy for Human Cancer. *Science* **2018**, *359*, 1361–1365.
- (6) Gubin, M. M.; Schreiber, R. D. The Odds of Immunotherapy Success. *Science* **2015**, *350*, 158–159.
- (7) Johnson, B. A., III; Yarchoan, M.; Lee, V.; Laheru, D. A.; Jaffee, E. M. Strategies for Increasing Pancreatic Tumor Immunogenicity. *Clin. Cancer Res.* **2017**, *23*, 1656–1669.
- (8) Feng, B.; Zhou, F.; Hou, B.; Wang, D.; Wang, T.; Fu, Y.; Ma, Y.; Yu, H.; Li, Y. Binary Cooperative Prodrug Nanoparticles Improve Immunotherapy by Synergistically Modulating Immune Tumor Microenvironment. *Adv. Mater.* **2018**, *30*, 1803001.
- (9) Kroemer, G.; Galluzzi, L.; Kepp, O.; Zitvogel, L. Immunogenic Cell Death in Cancer Therapy. *Annu. Rev. Immunol.* **2013**, *31*, 51–72.
- (10) Krysko, D. V.; Garg, A. D.; Kaczmarek, A.; Krysko, O.; Agostinis, P. P.; Vandenabeele, P. Immunogenic Cell Death and DAMPs in Cancer Therapy. *Nat. Rev. Cancer* **2012**, *12*, 860–875.
- (11) Galluzzi, L.; Buqué, A.; Kepp, O.; Zitvogel, L.; Kroemer, G. Immunogenic Cell Death in Cancer and Infectious Disease. *Nat. Rev. Immunol.* **2017**, *17*, 97–111.
- (12) Xu, J.; Xu, L.; Wang, C.; Yang, R.; Zhuang, Q.; Han, X.; Dong, Z.; Zhu, W.; Peng, R.; Liu, Z. Near-Infrared-Triggered Photodynamic Therapy with Multitasking Upconversion Nanoparticles in Combination with Checkpoint Blockade for Immunotherapy of Colorectal Cancer. *ACS Nano* **2017**, *11*, 4463–4474.
- (13) Chao, Y.; Xu, L.; Liang, C.; Feng, L.; Xu, J.; Dong, Z.; Tian, L.; Yi, X.; Yang, K.; Liu, Z. Combined Local Immunostimulatory Radioisotope Therapy and Systemic Immune Checkpoint Blockade Imparts Potent Antitumor Responses. *Nat. Biomed. Eng.* **2018**, *2*, 611–621.
- (14) Yang, Y.; Tang, J.; Abbaraju, P. L.; Jambhrunkar, M.; Song, H.; Zhang, M.; Lei, C.; Fu, J.; Gu, Z.; Liu, Y.; Yu, C. Hybrid Nanoreactors: Enabling an Off-the-Shelf Strategy for Concurrently Enhanced Chemo-immunotherapy. *Angew. Chem., Int. Ed.* **2018**, *57*, 11764–11769.
- (15) Li, J.; Cui, D.; Huang, J.; He, S.; Yang, Z.; Zhang, Y.; Luo, Y.; Pu, K. Organic Semiconducting Pro-nanostimulants for Near-Infrared Photoactivatable Cancer Immunotherapy. *Angew. Chem., Int. Ed.* **2019**, *58*, 12680–12687.
- (16) Li, J.; Huang, J.; Lyu, Y.; Huang, J.; Jiang, Y.; Xie, C.; Pu, K. Photoactivatable Organic Semiconducting Pro-nanoenzymes. *J. Am. Chem. Soc.* **2019**, *141*, 4073–4079.
- (17) Wen, M.; Ouyang, J.; Wei, C.; Li, H.; Chen, W.; Liu, Y.-N. Artificial Enzyme Catalyzed Cascade Reactions: Antitumor Immunotherapy Reinforced by NIR-II Light. *Angew. Chem., Int. Ed.* **2019**, *58*, 17425–17432.
- (18) Xu, B.; Cui, Y.; Wang, W.; Li, S.; Lyu, C.; Wang, S.; Bao, W.; Wang, H. M.; Qin, Z.; Liu, W.; Wei, H.; Liu, H. Immunomodulation-Enhanced Nanozyme-Based Tumor Catalytic Therapy. *Adv. Mater.* **2020**, *32*, 2003563.
- (19) Ding, B.; Zheng, P.; Jiang, F.; Zhao, Y.; Wang, M.; Chang, M.; Ma, P. a.; Lin, J. MnO_x Nanospikes as Nanoadjuvants and Immunogenic Cell Death Drugs with Enhanced Antitumor Immunity and Antimetastatic Effect. *Angew. Chem., Int. Ed.* **2020**, *59*, 16381–16384.
- (20) Duan, X.; Chan, C.; Lin, W. Nanoparticle-Mediated Immunogenic Cell Death Enables and Potentiates Cancer Immunotherapy. *Angew. Chem., Int. Ed.* **2019**, *58*, 670–680.
- (21) Nathan, C.; Cohn, Z. Antitumor Effects of Hydrogen Peroxide in vivo. *J. Exp. Med.* **1981**, *154*, 1539–1553.
- (22) Ben-Yoseph, O.; Ross, B. D. Oxidation Therapy: The Use of a Reactive Oxygen Species-Generating Enzyme System for Tumour Treatment. *Br. J. Cancer* **1994**, *70*, 1131–1135.
- (23) Sawa, T.; Wu, J.; Akaike, T.; Maeda, H. Tumor-targeting Chemotherapy by a Xanthine Oxidase-Polymer Conjugate That Generates Oxygen-free Radicals in Tumor Tissue. *Cancer Res.* **2000**, *60*, 666–671.
- (24) Fang, J.; Sawa, T.; Akaike, T.; Maeda, H. Tumor-targeted Delivery of Polyethylene Glycol-conjugated d-Amino Acid Oxidase for Antitumor Therapy via Enzymatic Generation of Hydrogen Peroxide. *Cancer Res.* **2002**, *62*, 3138–3143.
- (25) Sakuma, S.; Abe, M.; Kohda, T.; Fujimoto, Y. Hydrogen Peroxide Generated by Xanthine/Xanthine Oxidase System Represses the Proliferation of Colorectal Cancer Cell Line Caco-2. *J. Clin. Biochem. Nutr.* **2015**, *56*, 15–19.
- (26) Hao, H.; Sun, M.; Li, P.; Sun, J.; Liu, X.; Gao, W. In Situ Growth of a Cationic Polymer from the N-Terminus of Glucose Oxidase To Regulate H₂O₂ Generation for Cancer Starvation and H₂O₂ Therapy. *ACS Appl. Mater. Interfaces* **2019**, *11*, 9756–9762.
- (27) Zhao, W.; Hu, J.; Gao, W. Glucose Oxidase-Polymer Nanogels for Synergistic Cancer-Starving and Oxidation Therapy. *ACS Appl. Mater. Interfaces* **2017**, *9*, 23528–23535.
- (28) Fan, W.; Lu, N.; Huang, P.; Liu, Y.; Yang, Z.; Wang, S.; Yu, G.; Liu, Y.; Hu, J.; He, Q.; Qu, J.; Wang, T.; Chen, X. Glucose-Responsive Sequential Generation of Hydrogen Peroxide and Nitric Oxide for Synergistic Cancer Starving-Like/Gas Therapy. *Angew. Chem., Int. Ed.* **2017**, *56*, 1229–1233.
- (29) Chang, K.; Liu, Z.; Fang, X.; Chen, H.; Men, X.; Yuan, Y.; Sun, K.; Zhang, X.; Yuan, Z.; Wu, C. Enhanced Phototherapy by Nanoparticle-Enzyme via Generation and Photolysis of Hydrogen Peroxide. *Nano Lett.* **2017**, *17*, 4323–4329.
- (30) Huo, M.; Wang, L.; Chen, Y.; Shi, J. Tumor-Selective Catalytic Nanomedicine by Nanocatalyst Delivery. *Nat. Commun.* **2017**, *8*, 357.
- (31) Zhang, R.; Feng, L.; Dong, Z.; Wang, L.; Liang, C.; Chen, J.; Ma, Q.; Zhang, R.; Chen, Q.; Wang, Y.; Liu, Z. Glucose & Oxygen Exhausting Liposomes for Combined Cancer Starvation and Hypoxia-Activated Therapy. *Biomaterials* **2018**, *162*, 123–131.
- (32) Yang, Y.; Lu, Y.; Abbaraju, P. L.; Azimi, L.; Lei, C.; Tang, J.; Jambhrunkar, M.; Fu, J.; Zhang, M.; Liu, Y.; Liu, C.; Yu, C. Stepwise Degradable Nanocarriers Enabled Cascade Delivery for Synergistic Cancer Therapy. *Adv. Funct. Mater.* **2018**, *28*, 1800706.
- (33) Li, S.-Y.; Cheng, H.; Xie, B.-R.; Qiu, W.-X.; Zeng, J.-Y.; Li, C.-X.; Wan, S.-S.; Zhang, L.; Liu, W.-L.; Zhang, X.-Z. Cancer Cell Membrane Camouflaged Cascade Bioreactor for Cancer Targeted Starvation and Photodynamic Therapy. *ACS Nano* **2017**, *11*, 7006–7018.
- (34) Liu, W.; Ruan, M.-L.; Liu, L.; Ji, X.; Ma, Y.; Yuan, P.; Tang, G.; Lin, H.; Dai, J.; Xue, W. Self-Activated in Vivo Therapeutic Cascade of Erythrocyte Membrane-cloaked Iron-mineralized Enzymes. *Theranostics* **2020**, *10*, 2201–2214.
- (35) Xie, W.; Deng, W.-W.; Zan, M.; Rao, L.; Yu, G.-T.; Zhu, D.-M.; Wu, W.-T.; Chen, B.; Ji, L.-W.; Chen, L.; Liu, K.; Guo, S.-S.; Huang, H.-M.; Zhang, W.-F.; Zhao, X.; Yuan, Y.; Dong, W.; Sun, Z.-J.; Liu, W. Cancer Cell Membrane Camouflaged Nanoparticles to Realize Starvation Therapy Together with Checkpoint Blockades for Enhancing Cancer Therapy. *ACS Nano* **2019**, *13*, 2849–2857.
- (36) Li, Y.; Zhang, X.; Wan, X.; Liu, X.; Pan, W.; Li, N.; Tang, B. Inducing Endoplasmic Reticulum Stress to Expose Immunogens: A

DNA Tetrahedron Nanoregulator for Enhanced Immunotherapy. *Adv. Funct. Mater.* **2020**, *30*, 2000532.

(37) Chang, M.; Wang, M.; Wang, M.; Shu, M.; Ding, B.; Li, C.; Pang, M.; Cui, S.; Hou, Z.; Lin, J. A Multifunctional Cascade Bioreactor Based on Hollow-Structured Cu_2MoS_4 for Synergetic Cancer Chemo-Dynamic Therapy/Starvation Therapy/Phototherapy/Immunotherapy with Remarkably Enhanced Efficacy. *Adv. Mater.* **2019**, *31*, 1905271.

(38) Sindhvani, S.; Syed, A. M.; Ngai, J.; Kingston, B. R.; Maiorino, L.; Rothschild, J.; MacMillan, P.; Zhang, Y.; Rajesh, N. U.; Hoang, T.; Wu, J. L. Y.; Wilhelm, S.; Zilman, A.; Gadde, S.; Sulaiman, A.; Ouyang, B.; Lin, Z.; Wang, L.; Egeblad, M.; Chan, W. C. W. The Entry of Nanoparticles into Solid Tumours. *Nat. Mater.* **2020**, *19*, 566–575.

(39) Chiang, C.-W.; Liu, X.; Sun, J.; Guo, J.; Tao, L.; Gao, W. Polymerization-Induced Coassembly of Enzyme-Polymer Conjugates into Comicles with Tunable and Enhanced Cascade Activity. *Nano Lett.* **2020**, *20*, 1383–1387.

(40) Tsai, Y.-L.; Ha, D. P.; Zhao, H.; Carlos, A. J.; Wei, S.; Pun, T. K.; Wu, K.; Zandi, E.; Kelly, K.; Lee, A. S. Endoplasmic Reticulum Stress Activates SRC, Relocating Chaperones to The Cell Surface Where GRP78/CD109 Blocks TGF- β Signaling. *Natl. Acad. Sci.* **2018**, *115*, E4245–E4254.

(41) Prasad, M.; Pawlak, K. J.; Burak, W. E.; Perry, E. E.; Marshall, B.; Whittall, R. M.; Bose, H. S. Mitochondrial Metabolic Regulation by GRP78. *Sci. Adv.* **2017**, *3*, No. e1602038.

(42) He, C.; Duan, X.; Guo, N.; Chan, C.; Poon, C.; Weichselbaum, R. R.; Lin, W. Core-Shell Nanoscale Coordination Polymers Combine Chemotherapy and Photodynamic Therapy to Potentiate Checkpoint Blockade Cancer Immunotherapy. *Nat. Commun.* **2016**, *7*, 12499.

(43) Obeid, M.; Tesniere, A.; Ghiringhelli, F.; Fimia, G. M.; Apetoh, L.; Perfettini, J.-L.; Castedo, M.; Mignot, G.; Panaretakis, T.; Casares, N.; Métévier, D.; Larochette, N.; van Endert, P.; Ciccocanti, F.; Piacentini, M.; Zitvogel, L.; Kroemer, G. Calreticulin Exposure Dictates The Immunogenicity of Cancer Cell Death. *Nat. Med.* **2007**, *13*, 54–61.

(44) Sharma, P.; Allison, J. P. Immune Checkpoint Targeting in Cancer Therapy: Toward Combination Strategies with Curative Potential. *Cell* **2015**, *161*, 205–214.

(45) Wculek, S. K.; Cueto, F. J.; Mujal, A. M.; Melero, I.; Krummel, M. F.; Sancho, D. Dendritic Cells in Cancer Immunology and Immunotherapy. *Nat. Rev. Immunol.* **2020**, *20*, 7–24.

Recommended by ACS

Biodegradable Ferrous Sulfide-Based Nanocomposites for Tumor Theranostics through Specific Intratumoral Acidosis-Induced Metabolic Symbiosis Disruption

Jingjing Wang, Yanglong Hou, *et al.*

OCTOBER 02, 2022

JOURNAL OF THE AMERICAN CHEMICAL SOCIETY

READ 

Mitochondrial Dysfunction and Antioxidation Dyshomeostasis-Enhanced Tumor Starvation Synergistic Chemotherapy Achieved using a Metal–Organic Framework...

Taotao Huo, Rongqin Huang, *et al.*

JANUARY 12, 2022

ACS APPLIED MATERIALS & INTERFACES

READ 

Ascorbate Tumor Chemotherapy by An Iron-Engineered Nanomedicine-Catalyzed Tumor-Specific Pro-Oxidation

Bowen Yang and Jianlin Shi

DECEMBER 14, 2020

JOURNAL OF THE AMERICAN CHEMICAL SOCIETY

READ 

Engineering a pH/Glutathione-Responsive Tea Polyphenol Nanodevice as an Apoptosis/Ferroptosis-Inducing Agent

Min Mu, Gang Guo, *et al.*

JUNE 02, 2020

ACS APPLIED BIO MATERIALS

READ 

Get More Suggestions >